

Time-Correlated Window-Carrier-Phase-Aided GNSS Positioning Using Factor Graph Optimization for Urban Positioning

XIWEI BAI 
WEISONG WEN 
LI-TA HSU 

Hong Kong Polytechnic University, Hong Kong

This article proposes an improved global navigation satellite system (GNSS) positioning method that explores the time correlation between consecutive epochs of the code and carrier-phase measurements, which significantly increases the robustness against outlier measurements. Instead of relying on the time difference carrier phase which only considers two neighboring epochs using an extended Kalman filter estimator, this article proposed to employ the carrier-phase measurements inside a window, the so-called window carrier phase (WCP), to constrain the states inside a factor graph. A left null space matrix is employed to eliminate the shared unknown ambiguity variables and, therefore, correlate the associated states inside the WCP. Then, the pseudorange, Doppler, and the constructed WCP measurements are integrated simultaneously using factor graph optimization to estimate the state of the GNSS receiver. We evaluated the performance of the proposed method in two typical urban canyons in Hong Kong, achieving the mean positioning errors of 1.76 and 2.96 m, respectively, using the automobile-level GNSS receiver. Meanwhile, the effectiveness of the proposed method is further evaluated using a low-cost smartphone-level GNSS receiver, and similar improvement is also obtained when compared with several existing GNSS positioning methods.

Manuscript received August 12, 2021; revised November 30, 2021; released for publication February 2, 2022. Date of publication February 8, 2022; date of current version August 9, 2022.

DOI. No. 10.1109/TAES.2022.3149730

Refereeing of this contribution was handled by J. Seo.

This work was supported by the Hong Kong PolyU Startup Fund through the Resilient GNSS Positioning for Autonomous Aerial Vehicle in Urban Scenarios under Project BD63.

Authors' address: The authors are with the Department of Aero-nautical and Aviation Engineering, Polytechnic University, Hong Kong, E-mail: (xiwei.bai@connect.polyu.hk; welson.wen@polyu.edu.hk; lt.hsu@polyu.edu.hk). (Corresponding author: Weisong Wen.)

0018-9251 © 2022 IEEE

I. INTRODUCTION

The global navigation satellite system (GNSS) [1] is currently one of the major means of providing globally referenced positioning for autonomous systems [2]–[4] with navigation requirements. With the increased availability of multiple satellite constellations, GNSS can provide satisfactory performance in open-sky areas [5] based on the received pseudorange measurements via single-point positioning. However, the positioning accuracy is significantly degraded in highly urbanized cities, such as Hong Kong, due to signal reflection caused by static buildings and dynamic objects [6], such as double-decker buses, leading to the notorious nonlight-of-sight (NLOS) receptions and multipath effects, so-called outlier measurements or measurements with systematic errors [7], [8]. To mitigate the effects of the GNSS outlier measurements, numerous methods were proposed by introducing additional information or sensors, such as 3-D-mapping-aided GNSS [9]–[11], camera-aided GNSS NLOS detection [12]–[14], and 3-D-LiDAR-aided GNSS NLOS detection [6] or correction [12], [15]. Unfortunately, these methods rely on the availability of 3-D mapping information or LiDAR sensors, which are not suitable for low-cost applications.

The other research stream is to make use of the Doppler frequency or carrier-phase measurements to improve the robustness of the estimator against outlier measurements. The fusion of pseudorange and Doppler measurements [16] was studied using an extended Kalman filter (EKF). The Doppler measurement, which is less noisy compared with the pseudorange measurements, was employed to estimate the velocity of the GNSS receiver to further constrain the kinematic of the GNSS receiver together with the pseudorange measurements. Given the fact that the GNSS measurements are highly environmental dependent and time correlated [17], [18], the conventional filtering-based method (e.g., EKF estimator) for GNSS positioning cannot simultaneously explore the time correlation among historical measurements. As a result, the filtering-based estimator is still sensitive to unexpected outlier measurements. To fill this gap, our recent work [19] proposed a factor graph optimization (FGO)-based GNSS positioning method that integrates the pseudorange and Doppler frequency measurements, which makes use of the historical information to increase the robustness of the estimator. Improved accuracy is obtained in the evaluated datasets compared with the conventional EKF estimator. However, the potential of carrier-phase measurement with high accuracy was not explored in [19]. Compared with the pseudorange and the Doppler measurements, the carrier phase is less sensitive to the multipath effects [1], [20]. However, the received carrier-phase measurement involves an unknown integer ambiguity, which should be resolved for high-accuracy positioning that is commonly done in GNSS real-time kinematic (GNSS-RTK) positioning using the popular LAMBDA algorithm [21]. However, the GNSS-RTK requires additional continuous corrections from the nearby reference stations, which are not usually available. The PPP-RTK [22], which is a synthesis of precise

point positioning and network-based RTK concept, opened a new window for precise and flexible GNSS positioning. However, both the GNSS-RTK and the PPP-RTK require the resolution of the integer ambiguity variables.

One alternative to using the carrier phase is to make use of the time-difference carrier-phase (TDCP) [23]–[25] technique to eliminate the unknown integer ambiguity between the consecutive epochs. By differencing the carrier-phase measurements between two epochs based on the assumption that the integer ambiguity variables of the two consecutive epochs are the same, the derived TDCP displacements can be applied to constrain the position difference of the associated two epochs. Meanwhile, the TDCP displacements can also be used to estimate velocity by its derivation over time [23]. Considering that both the TDCP and the Doppler frequency can be applied to estimate the velocity, the team from the China University of Mining and Technology conducted continuous work to integrate both information to estimate the velocity of the GNSS receiver in [26]–[28]. Interestingly, the recent work by the team from the Chiba Institute of Technology proposed a reference-station-free double-difference technique to remove the integer ambiguity variables across all the epochs [29]. However, all these methods only consider the TDCP measurements in two epochs. According to the nature of GNSS tracking loops, the integer ambiguity tends to be constant once the satellite signal is effectively tracked. In other words, the signals transmitted from the same satellite that tracked in multiple epochs share the same ambiguity. Interestingly, this is similar to the visual-inertial integrated navigation system [30], where the visual landmarks share the same position (corresponding to the satellite ambiguity) in multiple epochs. In other words, the states in multiple epochs are strongly correlated with the visual landmarks tracked repetitively. To avoid the repetitive estimation of the position of the landmarks, Li and Mourikis [30] proposed to eliminate the shared variable (position) of the landmarks from the visual observation function to, therefore, increase the computational efficiency and guarantee the exploration of the time-correlation simultaneously. Based on a similar elimination operation, Zhao *et al.* [31] proposed to avoid the integer ambiguity resolution in the integration of GNSS-RTK and inertial measurement unit (IMU). However, its performance relies on the cost of the applied IMU sensor. Inspired by the elimination operation work presented in [30] and our previous work [19], this article proposes to employ the carrier-phase measurements received from the same satellite inside a window, the so-called window carrier-phase (WCP), to constrain the states inside a factor graph. Meanwhile, since these carrier-phase measurements share the same integer ambiguity variables, a left null space matrix is employed to eliminate the ambiguity variables and, therefore, correlate the associated states inside the window. By correlating the GNSS measurements within multiple epochs, the time correlation can be exploited simultaneously, leading to increased robustness against the outlier measurements. Furthermore, to cope with the potential inconsistency in integer ambiguity variables, the

M-estimator [32] is employed to mitigate the impacts of the cycle slip phenomenon. Then, the factor graph is employed to fuse the proposed WCP constraint, pseudorange, and the Doppler measurements for GNSS positioning. The main contributions of this article are listed as follows:

- 1) This article is a continuation of [19] by extending the deployment of the high-accuracy carrier-phase measurements via a WCP constraint, which enables exploration of the kinematic time correlation between multiple epochs, for single GNSS receiver positioning. Importantly, the conventional EKF estimator is not able to exploit the advantage of the proposed WCP since only the two consecutive epochs are considered due to its recursive form. Fortunately, the proposed factor-graph-based formulation opens a window for the utilization of the high-accuracy carrier-phase measurements.
- 2) This article verifies the effectiveness of the proposed method with several challenging datasets collected in the urban canyons of Hong Kong, via both automobile-level and smartphone-level GNSS receivers. Since the performance of the WCP is highly related to the size of the window, we analyze the impact of the window size on the performance of the proposed GNSS positioning. Moreover, the accommodation of the potential cycle slip, which can violate the assumption of shared integer ambiguity inside the WCP, is analyzed using the different setup of the M-estimator.

The rest of this article is organized as follows. An overview of the proposed method is given in Section II. Section III presents the modeling of the pseudorange, Doppler, and conventional TDCP and their integration using the FGO. The derivation of the proposed WCP constraint is elaborated together with the application of WCP in FGO in Section IV. Several real experiments were performed to evaluate the effectiveness of the proposed method in Section V. Finally, Section VI concludes this article.

II. OVERVIEW OF THE PROPOSED METHOD

An overview of the proposed method in this article is shown in Fig. 1. The inputs of the method are the raw pseudorange, Doppler frequency, and carrier-phase measurements from a GNSS receiver. The output is the state estimation of the GNSS receiver in the earth-centered, earth-fixed frame. The measurement modeling blocks remove the atmospheric and satellite clock errors involved in the raw measurements. Finally, three kinds of factors are integrated using FGO. In this article, matrices are denoted as uppercase with bold letters. Vectors are denoted as lowercase with bold letters. Variable scalars are denoted as lowercase italic letters. Constant scalars are denoted as lowercase letters. Moreover, the GNSS positioning mentioned in this article means the pseudorange and Doppler frequency measurement fusion using FGO, based on our previous work [19].

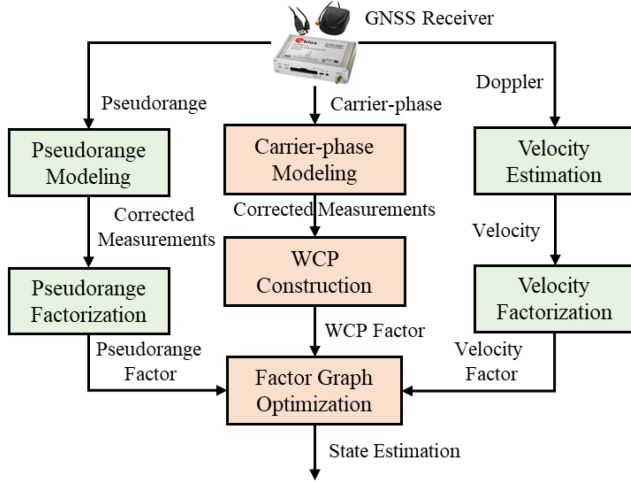


Fig. 1. Overview of the proposed method. The inputs are the continuous raw GNSS measurements. The output is the state estimation from the FGO.

This article focuses on employing the carrier phase to aid the GNSS positioning method.

To make the proposed pipeline clear, the following major notations are defined and followed in the rest of the article.

- 1) The pseudorange measurement received from a satellite s at a given epoch t is expressed as $\rho_{r,t}^s$. The subscript r denotes the GNSS receiver. The superscript s denotes the index of the satellite.
- 2) The Doppler measurement received from the satellite s at a given epoch t is expressed as $d_{r,t}^s$.
- 3) The carrier-phase measurement received from the satellite s at a given epoch t is expressed as $\psi_{r,t}^s$.
- 4) The position of the satellite s at a given epoch t is expressed as $\mathbf{p}_t^s = (p_{t,x}^s, p_{t,y}^s, p_{t,z}^s)^T$.
- 5) The velocity of the satellite s at a given epoch t is expressed as $\mathbf{v}_t^s = (v_{t,x}^s, v_{t,y}^s, v_{t,z}^s)^T$.
- 6) The position of the GNSS receiver at a given epoch t is expressed as $\mathbf{p}_{r,t} = (p_{r,t,x}, p_{r,t,y}, p_{r,t,z})^T$.
- 7) The velocity of the GNSS receiver at a given epoch t is expressed as $\mathbf{v}_{r,t} = (v_{r,t,x}, v_{r,t,y}, v_{r,t,z})^T$.
- 8) The clock bias of the GNSS receiver at a given epoch t is expressed as $\delta_{r,t}$ (unit, meter). $\delta_{r,t}^s$ denotes the satellite clock bias (unit, meter).

III. GNSS POSITIONING AIDED BY TDPC MEASUREMENTS

This section presents the methodology of the GNSS positioning aided by the TDPC measurement for further theoretical comparison between the conventional TDPC and the proposed WCP constraint (to be presented in Section IV). The utilization of TDPC is not original in the existing work using EKF [23]; however, this article still presents it for further theoretical and experimental comparison with the proposed WCP constraint. The state of the GNSS receiver is represented as follows:

$$\boldsymbol{\chi} = [\mathbf{x}_{r,1}, \mathbf{x}_{r,2}, \dots, \mathbf{x}_{r,n}] \quad (1)$$

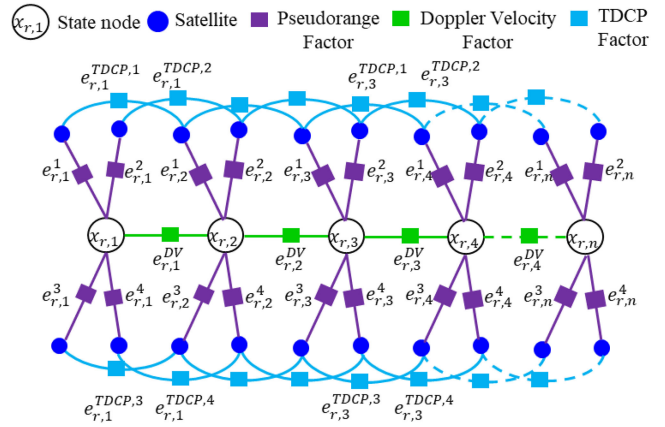


Fig. 2. Graph structure for a conventional pseudorange/Doppler/TDPC integration. The blue circle denotes the satellite. Only four satellites are drawn at each epoch for simplicity. The purple-shaded rectangle denotes the pseudorange factor (e.g., $e_{r,i}^s$). The green-shaded rectangle represents the Doppler velocity factor (e.g., $e_{r,i}^{DV}$). The light-blue-shaded rectangle denotes the TDPC factor. The white-shaded circle stands for the state of the GNSS receiver.

where the variable $\boldsymbol{\chi}$ denotes the set of states of the GNSS receiver ranging from the first epoch to the current epoch n . The state of the GNSS receiver at a single epoch can be denoted as follows:

$$\mathbf{x}_{r,t} = (\mathbf{p}_{r,t}, \mathbf{v}_{r,t}, \delta_{r,t})^T \quad (2)$$

where $\mathbf{x}_{r,t}$ denotes the state of the GNSS receiver at epoch t , $t \in (1, n)$, which involves the position ($\mathbf{p}_{r,t}$), velocity ($\mathbf{v}_{r,t}$), and receiver clock bias ($\delta_{r,t}$).

The graph structure of the FGO for solving the GNSS positioning aided by the TDPC measurement is shown in Fig. 2. The subscript n of the state node denotes the total epochs of measurements considered in the FGO. Each state in the factor graph is connected using the Doppler velocity factor. Note that the formulation of the GNSS pseudorange/Doppler integration using the FGO is first presented in our latest work [19]. However, we still present it here for the completeness of the derivation of the proposed integration in Section IV.

A. Pseudorange Measurement Modeling

The pseudorange measurement from the GNSS receiver, $\rho_{r,t}^s$, is denoted as follows [33]:

$$\rho_{r,t}^s = r_{r,t}^s + c_L (\delta_{r,t} - \delta_{r,t}^s) + I_{r,t}^s + T_{r,t}^s + \varepsilon_{r,t}^s \quad (3)$$

where $r_{r,t}^s$ is the geometric range between the satellite and the GNSS receiver. c_L denotes the speed of light. $I_{r,t}^s$ represents the ionospheric delay; $T_{r,t}^s$ indicates the tropospheric delay. $\varepsilon_{r,t}^s$ represents the errors caused by the multipath effects, NLOS receptions, receiver noise, antenna-phase-related noise. Meanwhile, the atmosphere effects ($T_{r,t}^s$ and $I_{r,t}^s$) are compensated using the conventional models (the Saastamoinen and Klobuchar models, respectively) presented in RTKLIB [34].

The observation model for GNSS pseudorange measurement from a given satellite s is represented as follows:

$$\rho_{r,t}^s = h_{r,t}^s (\mathbf{p}_{r,t}, \mathbf{p}_t^s, \delta_{r,t}) + \omega_{r,t}^s \quad (4)$$

with $h_{r,t}^s (\mathbf{p}_{r,t}, \mathbf{p}_t^s, \delta_{r,t}) = \|\mathbf{p}_t^s - \mathbf{p}_{r,t}\| + \delta_{r,t}$

where the variable $\omega_{r,t}^s$ stands for the noise associated with $\rho_{r,t}^s$. Therefore, we can get the error function ($\mathbf{e}_{r,t}^s$) for a given satellite measurement $\rho_{r,t}^s$ as follows:

$$\|\mathbf{e}_{r,t}^s\|_{\Sigma_{r,t}^s}^2 = \|\rho_{r,t}^s - h_{r,t}^s (\mathbf{p}_{r,t}, \mathbf{p}_t^s, \delta_{r,t})\|_{\Sigma_{r,t}^s}^2 \quad (5)$$

where $\Sigma_{r,t}^s$ denotes the covariance matrix. We calculate $\Sigma_{r,t}^s$ based on the satellite elevation angle and signal-to-noise ratio (SNR) and following the work presented in [35].

B. Doppler Measurement Modeling

Given the Doppler measurement ($d_{r,t}^1, d_{r,t}^2, \dots$) of each satellite at an epoch t , the velocity ($\mathbf{v}_{r,t}$) of the GNSS receiver can be calculated using the weighted least squares (WLS) method [36]. The detail of estimating the velocity of the GNSS receiver based on Doppler measurement can be found in our previous work [19]. Therefore, the observation model for the velocity ($\mathbf{v}_{r,t}$) is expressed as follows:

$$\mathbf{v}_{r,t}^{DV} = h_{r,t}^{DV} (\mathbf{x}_{r,t+1}, \mathbf{x}_{r,t}) + \omega_{r,t}^{DV} \quad (6)$$

$$\text{with } h_{r,t}^{DV} (\mathbf{x}_{r,t+1}, \mathbf{x}_{r,t}) = \begin{bmatrix} (p_{r,t+1,x} - p_{r,t,x}) / \Delta t \\ (p_{r,t+1,y} - p_{r,t,y}) / \Delta t \\ (p_{r,t+1,z} - p_{r,t,z}) / \Delta t \end{bmatrix}$$

where $\mathbf{v}_{r,t}^{DV}$ denotes the velocity measurements. The variable $\omega_{r,t}^{DV}$ denotes the noise associated with the velocity measurements. The variable Δt denotes the time difference between epoch t and epoch $t + 1$. Therefore, we can get the error function ($\mathbf{e}_{r,t}^{DV}$) for a given Doppler velocity measurement $\mathbf{v}_{r,t}^{DV}$ as follows:

$$\|\mathbf{e}_{r,t}^{DV}\|_{\Sigma_{r,t}^{DV}}^2 = \left\| \frac{\mathbf{v}_{r,t}^{DV} + \mathbf{v}_{r,t+1}^{DV}}{2} - h_{r,t}^{DV} (\mathbf{x}_{r,t+1}, \mathbf{x}_{r,t}) \right\|_{\Sigma_{r,t}^{DV}}^2 \quad (7)$$

where $\Sigma_{r,t}^{DV}$ denotes the covariance matrix corresponding to the Doppler velocity measurement. $\Sigma_{r,t}^{DV}$ is set as $\sigma_{DV} \mathbf{I}_{3 \times 3}$, where $\mathbf{I}_{3 \times 3}$ denotes the identity matrix with a size of 3×3 . The σ_{DV} is an experimentally determined scaling factor that is set to 0.6 in this article.

C. TDCP Measurement Modeling

In terms of the measurements from the GNSS receiver, each carrier-phase measurement, $\psi_{r,t}^s$, is represented as follows [33]:

$$\lambda \psi_{r,t}^s = r_{r,t}^s + c_L (\delta_{r,t} - \delta_{r,t}^s) - I_{r,t}^s + T_{r,t}^s + \lambda B_{r,t}^s + d\psi_{r,t}^s + \epsilon_{r,t}^s \quad (8)$$

where $B_{r,t}^s$ is the carrier-phase bias and is given as $B_{r,t}^s = \psi_{r,0,t} - \psi_{0,t}^s + N_{r,t}^s$. The variable λ denotes the carrier wavelength. The variable $d\psi_{r,t}^s$ denotes the carrier-phase correction term, including antenna phase offsets and variations, station displacement by earth tides, phase windup effect, and relativity correction on the satellite clock. The

detailed formulation of the carrier-phase correction can be found in [34]. $\epsilon_{r,t}^s$ represents the errors caused by the multi-path effects, NLOS receptions, receiver noise, and antenna delay. The variable $\psi_{r,0,t}$ represents the initial phase of the receiver local oscillator. Similarly, $\psi_{0,t}^s$ stands for the initial phase of the transmitted navigation signal from the satellite. The variable $N_{r,t}^s$ denotes the carrier-phase integer ambiguity. Typically, $N_{r,t}^s$ is an unknown variable to be estimated during the utilization of the carrier-phase measurements. By differencing the raw carrier-phase measurements between two epochs, the TDCP measurement ($\Delta \lambda \psi_{r,t,t+1}^s$) can be derived as follows:

$$\begin{aligned} \Delta \lambda \psi_{r,t,t+1}^s &= (r_{r,t+1}^s - r_{r,t}^s) + c_L (\delta_{r,t+1} - \delta_{r,t}) \\ &\quad + (\epsilon_{r,t+1}^s - \epsilon_{r,t}^s) \end{aligned} \quad (9)$$

where the unknown integer ambiguity term is eliminated by the differencing operation. Therefore, the observation model for the TDCP measurement from a given satellite s is represented as follows:

$$\begin{aligned} \Delta \lambda \psi_{r,t,t+1}^s &= h_{r,t}^{TDCP,s} (\mathbf{p}_{r,t}, \mathbf{p}_t^s, \delta_{r,t}, \mathbf{p}_{r,t+1}, \mathbf{p}_{t+1}^s, \delta_{r,t+1}) \\ &\quad + \omega_{r,t}^{TDCP,s} \end{aligned} \quad (10)$$

with $h_{r,t}^{TDCP,s} (\mathbf{p}_{r,t}, \mathbf{p}_t^s, \delta_{r,t}, \mathbf{p}_{r,t+1}, \mathbf{p}_{t+1}^s, \delta_{r,t+1}) = (\|\mathbf{p}_t^s - \mathbf{p}_{r,t}\| + \delta_{r,t}) - (\|\mathbf{p}_{t+1}^s - \mathbf{p}_{r,t+1}\| + \delta_{r,t+1})$ where the variable $\omega_{r,t}^{TDCP,s}$ stands for the noise associated with the TDCP measurement. Therefore, we can get the error function ($\mathbf{e}_{r,t}^{TDCP,s}$) for the given TDCP measurements ($\psi_{r,t}^s, \psi_{r,t+1}^s$) as follows, (11) shown at the bottom of the next page, where $\Sigma_{r,t}^{TDCP,s}$ denotes the covariance matrix. Similarly, we calculate the $\Sigma_{r,t}^{TDCP,s}$ based on the satellite elevation angle and SNR and following the work presented in [35].

D. Pseudorange/Doppler/TDCP Fusion via FGO

Based on the factors derived above, the combined objective function can be formulated as follows, (12) shown at the bottom of the next page.

The variable χ^* denotes the optimal estimation of the state sets, which can be estimated by solving the objective function mentioned above iteratively. The operator $\rho(*)$ denotes the robust function of the M-estimator [32].

IV. GNSS POSITIONING AIDED BY WCP

This section presents the methodology of the GNSS positioning aided by the proposed WCP constraint. The graph structure of the FGO for solving the GNSS positioning aided by the WCP constraint is shown in Fig. 3, where the TDCP in Fig. 2 is replaced by the proposed WCP.

A. WCP Constraint Modeling

Fig. 3 shows that four satellites (satellites 1–4) are received repetitively from epoch 1 to epoch n , which are involved in the factor graph.

Taking satellite 1 as an example, the continuous observed carrier-phase measurements can be stacked into the

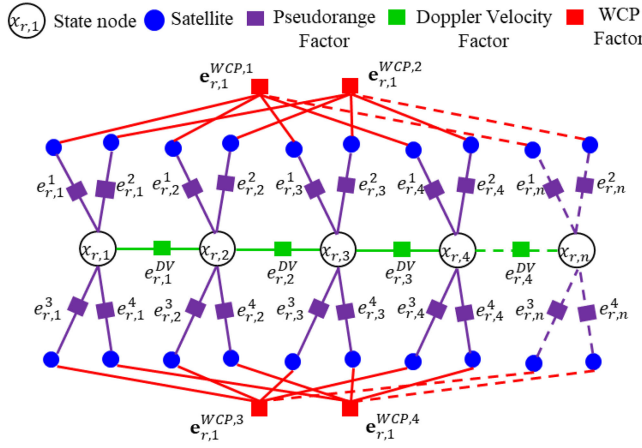


Fig. 3. Graph structure for the proposed pseudorange/Doppler/WCP integration. The blue circles denote the satellite. The purple-shaded rectangle denotes the pseudorange factor (e.g., $e_{r,t}^s$). The green-shaded rectangle represents the Doppler velocity factor (e.g., $e_{r,t}^{DV}$). The red-shaded rectangle denotes the WCP factor. The white-shaded circle stands for the state of the GNSS receiver.

following form:

$$\begin{bmatrix} \lambda\psi_{r,1}^1 \\ \lambda\psi_{r,2}^1 \\ \dots \\ \lambda\psi_{r,N_k^s}^1 \end{bmatrix} = \begin{bmatrix} r_{r,t}^s + m_{r,t}^s \\ r_{r,2}^s + m_{r,2}^s \\ \dots \\ r_{r,N_k^s}^s + m_{r,N_k^s}^s \end{bmatrix} + \begin{bmatrix} \lambda B_{r,1}^s \\ \lambda B_{r,2}^s \\ \dots \\ \lambda B_{r,N_k^s}^s \end{bmatrix} + \begin{bmatrix} \epsilon_{r,1}^s \\ \epsilon_{r,2}^s \\ \dots \\ \epsilon_{r,N_k^s}^s \end{bmatrix} \quad (13)$$

with $m_{r,t}^s = c_L(\delta_{r,t} - \delta_{r,t}^s) - I_{r,t}^s + T_{r,t}^s + d\psi_{r,t}^s$, where N_k^s indicates that satellite 1 is tracked by the GNSS receiver continuously for N_k^s epochs. The carrier-phase measurements involved in (13) form a WCP of satellite 1 with a window size of N_k^s . The variable k denotes the index of the WCP constraint inside the factor graph. $m_{r,t}^s$ is defined for simplicity.

Given the fact that the carrier-phase measurements inside the window share the same integer ambiguity, (13) can be rewritten as follows:

$$\begin{bmatrix} \lambda\psi_{r,1}^1 \\ \lambda\psi_{r,2}^1 \\ \dots \\ \lambda\psi_{r,N_k^s}^1 \end{bmatrix} = \begin{bmatrix} r_{r,t}^s + m_{r,1}^s \\ r_{r,2}^s + m_{r,2}^s \\ \dots \\ r_{r,N_k^s}^s + m_{r,N_k^s}^s \end{bmatrix} + \lambda B_{r,N_k^s}^s \begin{bmatrix} 1 \\ 1 \\ \dots \\ 1 \end{bmatrix} + \begin{bmatrix} \epsilon_{r,1}^s \\ \epsilon_{r,2}^s \\ \dots \\ \epsilon_{r,N_k^s}^s \end{bmatrix} \quad (14)$$

where $B_{r,N_k^s}^s$ denotes the shared integer ambiguity value for satellite 1 within the continuous N_k^s epochs. The compact form of (14) can be further organized by multiplying a left null space matrix $\mathbf{G}_{r,k}^s$ on both sides of (14), and the

following form is obtained:

$$\mathbf{G}_{r,k}^s \begin{bmatrix} \lambda\psi_{r,1}^1 \\ \lambda\psi_{r,2}^1 \\ \dots \\ \lambda\psi_{r,N_k^s}^1 \end{bmatrix} = \mathbf{G}_{r,k}^s \begin{bmatrix} r_{r,t}^s + m_{r,1}^s \\ r_{r,2}^s + m_{r,2}^s \\ \dots \\ r_{r,N_k^s}^s + m_{r,N_k^s}^s \end{bmatrix} + \mathbf{G}_{r,k}^s \begin{bmatrix} \epsilon_{r,1}^s \\ \epsilon_{r,2}^s \\ \dots \\ \epsilon_{r,N_k^s}^s \end{bmatrix} \quad (15)$$

with $\mathbf{G}_{r,k}^s \begin{bmatrix} 1 \\ 1 \\ \dots \\ 1 \end{bmatrix} = \begin{bmatrix} 0 \\ 0 \\ \dots \\ 0 \end{bmatrix}$.

Therefore, (15) is free of the ambiguity variable, which is eliminated by a left multiplication of the left null space matrix $\mathbf{G}_{r,k}^s$. The construction of the $\mathbf{G}_{r,k}^s$ can be found in Appendix A.

Therefore, the observation model for WCP constraint from a given satellite s being tracked by N_k^s epochs are represented as follows:

$$\mathbf{G}_{r,k}^s \begin{bmatrix} \lambda\psi_{r,1}^1 \\ \lambda\psi_{r,2}^1 \\ \dots \\ \lambda\psi_{r,N_k^s}^1 \end{bmatrix} = \mathbf{G}_{r,k}^s \begin{bmatrix} h_{r,1}^{WCP,s}(\mathbf{p}_{r,1}, \mathbf{p}_1^s, \delta_1) \\ h_{r,2}^{WCP,s}(\mathbf{p}_{r,2}, \mathbf{p}_2^s, \delta_2) \\ \dots \\ h_{r,N_k^s}^{WCP,s}(\mathbf{p}_{r,N_k^s}, \mathbf{p}_{N_k^s}^s, \delta_{N_k^s}) \end{bmatrix} + \mathbf{G}_{r,k}^s \begin{bmatrix} \epsilon_{r,1}^s \\ \epsilon_{r,2}^s \\ \dots \\ \epsilon_{r,N_k^s}^s \end{bmatrix} \quad (16)$$

$$\text{with } h_{r,N_k^s}^{WCP,s}(\mathbf{p}_{r,N_k^s}, \mathbf{p}_{N_k^s}^s, \delta_{1,N_k^s}) = \|\mathbf{p}_{N_k^s}^s - \mathbf{p}_{r,N_k^s}\| + \delta_{1,N_k^s}.$$

Therefore, we can get the error function ($\mathbf{e}_{r,k}^{WCP,s}$) for a WCP constraint as follows, (17) shown at the bottom of the next page, where $\Sigma_{r,k}^{WCP,s}$ denotes the covariance matrix associated with the WCP constraint, which can be calculated as follows:

$$\Sigma_{r,k}^{WCP,s} = \mathbf{G}_{r,k}^s \begin{bmatrix} \epsilon_{r,1}^s & 0 & 0 & 0 \\ 0 & \epsilon_{r,2}^s & 0 & 0 \\ 0 & 0 & \dots & 0 \\ 0 & 0 & 0 & \epsilon_{r,N_k^s}^s \end{bmatrix} \mathbf{G}_{r,k}^{sT}. \quad (18)$$

The WCP factor ($\mathbf{e}_{r,k}^{WCP,s}$) is denoted by the red-shaded rectangles in Fig. 3, which connects the same satellite received in multiple epochs across the factor graph.

B. Comparison Between the Conventional TDCP and the Proposed WCP

Different from the conventional TDCP constraint that only explores the kinematic correlation between the two

$$\|\mathbf{e}_{r,t}^{TDCP,s}\|_{\Sigma_{r,t}^{TDCP,s}}^2 = \|\Delta\lambda\psi_{r,t+1}^s - h_{r,t}^{TDCP,s}(\mathbf{p}_{r,t}, \mathbf{p}_t^s, \delta_{r,t}, \mathbf{p}_{r,t+1}, \mathbf{p}_{t+1}^s, \delta_{r,t+1})\|_{\Sigma_{r,t}^{TDCP,s}}^2 \quad (11)$$

$$\chi^* = \arg \min_{\chi} \sum_{s,t} \left(\|\mathbf{e}_{r,t}^{DV}\|_{\Sigma_{r,t}^{DV}}^2 + \|\mathbf{e}_{r,t}^s\|_{\Sigma_{r,t}^s}^2 + \|\rho(\mathbf{e}_{r,t}^{TDCP,s})\|_{\Sigma_{r,t}^{TDCP,s}}^2 \right) \quad (12)$$

consecutive epochs, the proposed WCP constraint effectively makes use of the correlation of shared integer ambiguity within multiple epochs inside the window. Meanwhile, the involved covariance matrix ($\Sigma_{r,k}^{WCP,s}$) effectively maintained the cross-correlation using the multiplication of $\mathbf{G}_{r,k}^s$. Specifically, a similar format of the formulation can also be derived for TDGP measurements given a set of continuously tracked GNSS measurements from the same satellite as follows:

$$\begin{bmatrix} \Delta\lambda\psi_{r,1}^1 \\ \Delta\lambda\psi_{r,2}^1 \\ \dots \\ \Delta\lambda\psi_{r,N_k^s}^1 \end{bmatrix} = \mathbf{D}_{r,k}^s \begin{bmatrix} r_{r,t}^s + m_{r,1}^s \\ r_{r,2}^s + m_{r,2}^s \\ \dots \\ r_{r,N_k^s}^s + m_{r,N_k^s}^s \end{bmatrix} + \mathbf{D}_{r,k}^s \begin{bmatrix} \lambda B_{r,1}^s \\ \lambda B_{r,2}^s \\ \dots \\ \lambda B_{r,N_k^s}^s \end{bmatrix} + \mathbf{D}_{r,k}^s \begin{bmatrix} \epsilon_{r,1}^s \\ \epsilon_{r,2}^s \\ \dots \\ \epsilon_{r,N_k^s}^s \end{bmatrix} \quad (19)$$

where $\Delta\lambda\psi_{r,1}^1$ denotes the TDGP measurements of satellite 1. $\mathbf{D}_{r,k}^s$ denotes the time difference matrix, which is employed to remove the ambiguity term in the TDGP operation, and can be denoted as follows (five continuously tracked GNSS measurements as an example):

$$\mathbf{D}_{r,k}^s = \begin{bmatrix} -1 & 1 & 0 & 0 & 0 \\ 0 & -1 & 1 & 0 & 0 \\ 0 & 0 & -1 & 1 & 0 \\ 0 & 0 & 0 & -1 & 1 \\ 0 & 0 & 0 & 0 & 0 \end{bmatrix}. \quad (20)$$

The $\mathbf{D}_{r,k}^s$ matrix is sparse and only enables the time difference between consecutive epochs, which is the major difference between the TDGP and the proposed WCP. In other words, the TDGP can be a special format of the WCP constraint with a window size of 2. The analysis of the matrix $\mathbf{G}_{r,k}^s$, which is a densely correlated matrix, and $\mathbf{D}_{r,k}^s$ with real data is presented in Section V.

C. Cycle Slip Accommodation and Selection of the Window Size of the WCP

1) *Cycle Slip Accommodation*: In typical urban canyons, the occasional GNSS signal blockage and reflection can cause the cycle slip problem, which can therefore violate the assumption of shared integer ambiguity inside a WCP. From the measurement domain, the cycle slip phenomenon can cause significant inconsistency in the consecutive carrier-phase measurements. Thanks to the FGO, which involves a large number of redundant measurements, this article employs the robust M-estimator [32]

to detect and mitigate the effects of the cycle slip. Our previous work [37] shows that the M-estimator can effectively mitigate the unexpected visual outlier measurements in a visual/inertial integrated positioning system. A more detailed discussion about the cycle slip mitigation analysis using the M-estimator can be found in Section V.

2) *Window Size Selection of the WCP*: Theoretically, the best window size (N_k^s) of the WCP can be selected by maximizing the exploration of the time correlation of the states involved. Therefore, it is good to select the largest window size as long as the assumption of constant integer ambiguity inside the WCP holds. However, the invariant ambiguity inside the WCP for a long period is hard to satisfy in urban canyons due to the potential cycle slip. In other words, the integer ambiguity may not be the same within a long period (for example, 100 epochs). Therefore, we set a threshold for N_k^s denoted by $N_{k,MAX}^s$. For example, if satellite 1 was tracked continuously for $N_{k,MAX}^s + 4$ epochs, two different WCP constraints would be constructed, where the sizes are $N_{k,MAX}^s$ and 4, respectively.

D. Pseudorange/Doppler/WCP Fusion via FGO

Based on the factors derived above, the combined objective function proposed in this article can be formulated as follows:

$$\chi^* = \arg \min_{\chi} \sum_{s,t,k} \left(\|\mathbf{e}_{r,t}^{DV}\|_{\Sigma_{r,t}^{DV}}^2 + \|\mathbf{e}_{r,t}^s\|_{\Sigma_{r,t}^s}^2 + \left\| \rho \left(\mathbf{e}_{r,k}^{WCP,s} \right) \right\|_{\Sigma_{r,k}^{WCP,s}}^2 \right). \quad (21)$$

The variable χ^* denotes the optimal estimation of the state sets, which can be estimated by solving the objective function mentioned above iteratively. The operator $\rho(*)$ denotes the robust function of the M-estimator [32]; by applying the Cauchy function, it can be formulated as follows:

$$\rho \left(\mathbf{e}_{r,k}^{WCP,s} \right) = \frac{k_\rho}{2} \log \left(1 + \frac{\left(\mathbf{e}_{r,k}^{WCP,s} \right)^2}{k_\rho^2} \right) \quad (22)$$

where k_ρ denotes the kernel value (parameter) that dominates the nonconvexity of the Cauchy function. Meanwhile, the performance of the Cauchy function relies heavily on the selection of k_ρ , and the analysis is presented in Section V. Both the objectives (12) and (21) are solved using the Levenberg–Marquardt algorithm via the state-of-the-art Ceres-solver [38].

$$\left\| \mathbf{e}_{r,k}^{WCP,s} \right\|_{\Sigma_{r,k}^{WCP,s}}^2 = \left\| \mathbf{G}_{r,k}^s \begin{bmatrix} \lambda\psi_{r,1}^1 \\ \lambda\psi_{r,2}^1 \\ \dots \\ \lambda\psi_{r,N_k^s}^1 \end{bmatrix} - \mathbf{G}_{r,k}^s \begin{bmatrix} h_{r,1}^{WCP,s}(\mathbf{p}_{r,1}, \mathbf{p}_1^s, \delta_1) \\ h_{r,2}^{WCP,s}(\mathbf{p}_{r,2}, \mathbf{p}_2^s, \delta_2) \\ \dots \\ h_{r,N_k^s}^{WCP,s}(\mathbf{p}_{r,N_k^s}, \mathbf{p}_{N_k^s}^s, \delta_{N_k^s}) \end{bmatrix} \right\|_{\Sigma_{r,k}^{WCP,s}}^2 \quad (17)$$



Fig. 4. Demonstration of the evaluated urban canyons 1 and 2. The red curves denote the trajectories of the tests.

V. EXPERIMENT RESULTS AND DISCUSSION

A. Experiment Setup

1) *Experimental Scenes*: To verify the effectiveness of the proposed method, two experiments were conducted in typical urban canyons in Hong Kong. Fig. 4 shows the data collection vehicle [see Fig. 4(a)] and scenes in urban canyons 1 [see Fig. 4(b)] and 2 [see Fig. 4(c)]. Both of the urban scenarios contain static buildings, trees, and dynamic objects, such as double-decker buses, which can lead to numerous GNSS outlier measurements.

2) *Sensor Setups*: Fig. 4(a) shows the data collection vehicle, and the detail of the data collection vehicle can be found through our open-sourced UrbanNav [39] dataset.¹ In both experiments, a u-blox M8T GNSS receiver was used to collect raw GNSS measurements of GPS/Beidou at a frequency of 1 Hz. Meanwhile, the receiver clock bias of GPS and Beidou satellite systems is estimated separately in (5). Besides, the NovAtel SPAN-CPT, a GNSS (GPS, GLONASS, and Beidou) RTK/inertial navigation system (INS) (fiber-optic gyroscopes, FOG) integrated navigation system was used to provide ground truth of positioning. The gyro bias in-run stability of the FOG is 1° per hour, and its random walk is 0.067° per hour. The baseline between the rover and the GNSS base station is about 7 km. Meanwhile, we postprocess the data from SPAN-CPT using the inertial explorer software from NovAtel to guarantee the accuracy of the ground truth of positioning. All the data were collected and synchronized using a robot operating system (ROS) [40]. The coordinate systems between all the sensors were calibrated before the experiments.

3) *Evaluation Metrics*: We analyze the performance of positioning by comparing five different methods, as shown below, to validate the effectiveness of the proposed method in improving GNSS positioning. Note that the M-estimator is applied to both the TDCP and WCP constraints.

- 1) *u-blox* [41]: the commercial GNSS positioning solution from the u-blox M8T receiver.
- 2) *WLS* [34]: weighted least squares positioning.

TABLE I
Performance of the Listed Five Methods in Urban Canyon 1

Item (m)	u-blox	WLS	Sol 1	Sol 2	Sol 3
MEAN	6.23	3.10	2.14	2.01	1.76
STD	7.31	1.95	1.01	0.82	0.57
Max	38.53	11.23	6.52	5.69	4.06

Note: Max: maximum error; STD: standard deviation; MEAN: mean error; Sol 1: PSR-DOP; Sol 2: PSR-DOP-TDCP; Sol 3: PSR-DOP-WCP.

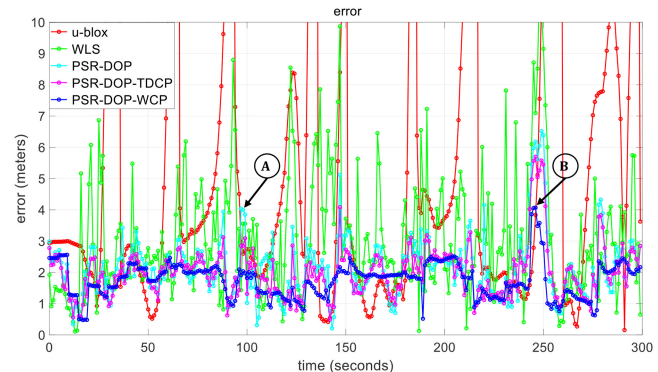


Fig. 5. Two-dimensional positioning errors of the evaluated five methods in urban canyon 1. The red curve denotes the 2-D error from the commercial solution of the u-blox receiver. The green, cyan, magenta, and blue colors denote the WLS, PSR-DOP, PSR-DOP-TDCP, and PSR-DOP-WCP, respectively.

- 3) *PSR-DOP (Sol 1)*: the pseudorange and Doppler integration using FGO based on the work presented in [19].
- 4) *PSR-DOP-TDCP (Sol 2)*: the pseudorange, Doppler, and TDCP measurements integration using FGO (corresponding to the factor graph in Fig. 2).
- 5) *PSR-DOP-WCP (Sol 3)*: the pseudorange, Doppler, and WCP measurements integration using FGO (corresponding to the factor graph presented in Fig. 3) with a maximum window size ($N_{k,MAX}^s$) of 6.

B. Experimental Evaluation in Urban Canyon 1

1) *Positioning Performance Evaluation*: The positioning results of the listed five methods are shown in Table I. The first column shows the 2-D positioning error of the u-blox receiver. The positioning result is based on standard NMEA [42] messages from the u-blox receiver. A mean error of 6.23 m was obtained, with a standard deviation of 7.31 m. The maximum error reached 38.53 m. The second column shows the positioning result using the raw pseudorange measurements from the u-blox receiver and positioning based on WLS. Similarly, the weighting scheme was taken from [35] and is based on the satellite elevation angle and the SNR. The positioning error decreased to 3.10 m with a standard deviation of 1.95 m. The maximum error also decreased to about 11 m. Fig. 5 shows the positioning error throughout the evaluation, where red and green colors denote the solutions from u-blox and WLS, respectively. The positioning error fluctuates occasionally during the test

¹[Online]. Available: <https://github.com/weisongwen/UrbanNavDataset>

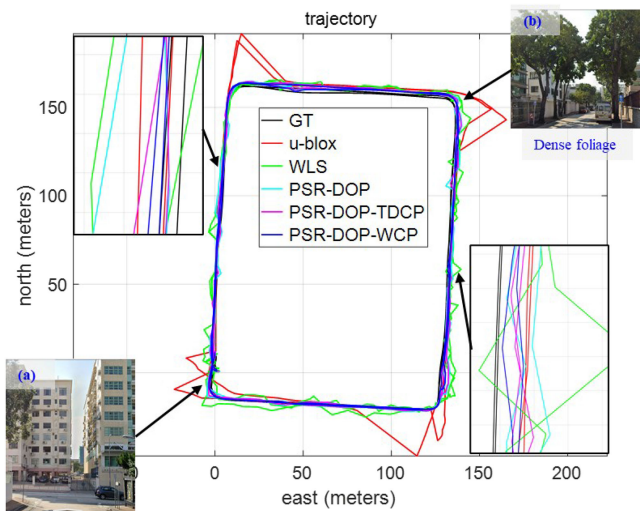


Fig. 6. Two-dimensional positioning trajectories of the evaluated five methods in urban canyon 1. The black and red curves denote the 2-D trajectories of the ground truth and the commercial solution of the u-blox receiver. The green, cyan, magenta, and blue colors denote the WLS, PSR-DOP, PSR-DOP-TDCP, and PSR-DOP-WCP, respectively.

due to the unexpected GNSS outlier measurements arising from the blockage and reflections by surrounding buildings.

With the help of the integration of the Doppler frequency measurements, the positioning error decreases to 2.14 m with the standard deviation decreasing to 1.01 m. The improved results show that the Doppler frequency measurement can help to mitigate the effects of the GNSS outlier measurements, which can also be seen in Fig. 5 with a smoother error curve by the method of PSR-DOP. However, the jump can still be seen (e.g., epoch A annotated by the circle in Fig. 5) as the Doppler measurement can also be biased by the multipath effects [43]. After applying the carrier-phase measurements using the TDCP technique (corresponding to the factor graph in Fig. 2), the positioning error decreases slightly to 2.01 m (PSR-DOP-TDCP) with a maximum error of 5.69 m. However, a more significant improvement can be seen in the standard deviation, which means that smoother results are obtained. The results show that the high-accuracy carrier-phase measurements can help to smooth the positioning against GNSS outlier measurements.

With the help of the proposed WCP constraint (corresponding to the factor graph in Fig. 3), the positioning error decreases to only 1.76 m, which is almost a lane-level accuracy and shows the effectiveness of the proposed method. Moreover, the standard deviation decreases to only 0.57 m with a maximum error of 4.06 m. The significantly decreased standard deviation indicates that the proposed WCP constraint can effectively constrain the multiple states more tightly compared with the TDCP, which only involves the two pairwise states. Fig. 6 shows the trajectories of the evaluated five methods. Epoch B in Fig. 5 is corresponding to Fig. 6(a) located in an intersection with tall buildings. As a result, the positioning error of the WLS is larger than 10 m. With the help of the WCP, the error decreases from 5.6

TABLE II
Performance of the Proposed Method Under Different Maximum Window Size ($N_{k,\text{MAX}}^s$) Assumptions

$N_{k,\text{MAX}}^s$	6	9	16	25	35
MEAN (m)	1.76	1.69	1.82	1.89	1.93
STD (m)	0.57	0.48	0.62	0.72	0.82
Max (m)	4.06	3.16	4.67	5.43	6.01

m for PSR-DOP-TDCP to only 4.06 m. Fig. 6(b) shows a scene with dense foliage, which can cause GNSS signal blockage and diffractions. As a result, the solution from WLS deviates significantly from the ground truth. However, smooth results are still achieved with the proposed method (PSR-DOP-WCP).

In short, both the Doppler frequency and the carrier-phase measurements can help to improve the positioning accuracy by mitigating the impacts of the GNSS outlier measurements. We gradually compare the improvement from both measurements. The utilization of the TDCP (PSR-DOP-TDCP) obtains similar accuracy compared with the PSR-DOP although with a slight decrease in standard deviation (STD) in the evaluated dataset. Fortunately, the proposed method (PSR-DOP-WCP) pushes the positioning performance to a higher accuracy with a mean error of 1.76 m and an STD of only 0.57 m.

2) *Analysis of the Impact of the Maximum Window Size:* Since the proposed WCP constraint is highly related to the maximum window size ($N_{k,\text{MAX}}^s$), Table II shows how $N_{k,\text{MAX}}^s$ impacts the performance of the overall integration (PSR-DOP-WCP). Therefore, we present the accuracy of the PSR-DOP-WCP under the different values of $N_{k,\text{MAX}}^s$. The maximum window size of 6 corresponds to the evaluation presented in Section V-B(1). Interestingly, after slightly increasing $N_{k,\text{MAX}}^s$, both the mean and standard deviation decrease, with the mean error decreasing from 1.76 to 1.69 m. This is due to fact that a larger $N_{k,\text{MAX}}^s$ enables a stronger correlation between the states. However, after almost doubling $N_{k,\text{MAX}}^s$, the mean error slightly increased to 1.82 m. A similar phenomenon is also seen by increasing $N_{k,\text{MAX}}^s$ to 25 and 35, respectively. This is caused by the violation of shared ambiguity variables inside the WCP due to the cycle slip. Although the proposed method in this article employs the M-estimator to mitigate the effects of the cycle slip, the error caused still exists.

Fig. 7 shows the details of the errors under different values of $N_{k,\text{MAX}}^s$. The representative epoch is epoch A (denoted by a circle in Fig. 7), where the green curve ($N_{k,\text{MAX}}^s = 9$) obtains better accuracy than all other methods. In addition to $N_{k,\text{MAX}}^s$, the maximum size of the WCP can also be determined by the times that one satellite is being tracked. The histograms [see Fig. 7(a) and (b)] denote the distributions of the window size of the WCP during two tests. It is shown that the majority of the WCP can have a size of $N_{k,\text{MAX}}^s$. However, N_k^s of some satellites is even smaller than 10 due to losing track occasionally. In short, the performance of the WCP constraint is highly related to the window size; however, too large size does not necessarily

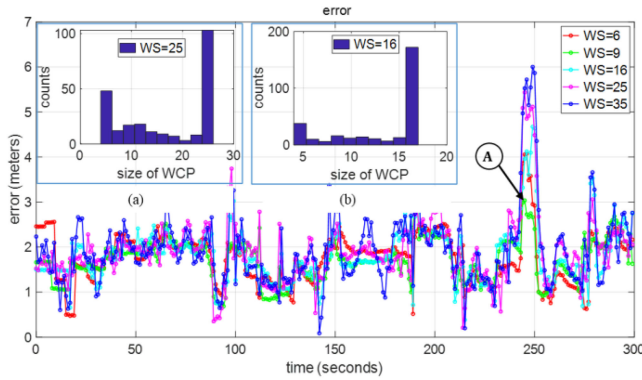


Fig. 7. Two-dimensional positioning errors of the proposed method under the different values of $N_{k,MAX}^s$. The “WS” in the legend denotes $N_{k,MAX}^s$. The x -axis denotes time, and the y -axis represents the errors.

TABLE III
Performance of the Listed Five Methods in Urban Canyon 2

Item (m)	u-blox	WLS	Sol 1	Sol 2	Sol 3
MEAN	31.02	16.66	3.90	5.21	2.96
STD	37.69	12.82	2.29	2.38	1.89
Max	177.6	56.23	12.84	12.52	12.02

Note: Max: maximum error; STD: standard deviation; MEAN: mean error; Sol 1: PSR-DOP; Sol 2: PSR-DOP-TDCP; Sol 3: PSR-DOP-WCP.

lead to better results due to the existence of occasional cycle slips.

C. Experimental Evaluation in Urban Canyon 2

1) *Positioning Performance Evaluation:* To challenge the performance of the proposed method, another experiment was conducted in a denser urban canyon 2 with significantly higher building structures. Table III shows that a mean error of 31.02 m is achieved via the commercial solution from the u-blox receiver. Similar to the experimental results in urban canyon 1, improved accuracy is obtained by the WLS, with the mean error decreasing to 16.66 m. Fortunately, the integration of the pseudorange and Doppler measurements using FGO (PSR-DOP) significantly reduces the error to only 3.9 m with a significantly decreased standard deviation. Interestingly, the utilization of the TDCP constraint even degrades the overall performance, with the mean error increasing to 5.21 m. This is due to the significantly increased percentage of the cycle slip phenomenon in urban canyons 2 with denser building structures. As a result, the TDCP becomes an incorrect constraint due to the violation of the constant integer ambiguity between consecutive epochs of measurements. However, after applying the proposed WCP, the mean error decreases to only 2.96 m with the standard deviation decreasing to only 1.89 m. The detailed 2-D positioning errors of the evaluated five methods are also shown in Fig. 8. Different from the TDCP, the WCP involves multiple carrier-phase measurements, and the impacts of the single-cycle slip can be further resisted by the measurement redundancy of the window constraint. This significant improvement again shows the effectiveness of the proposed method in

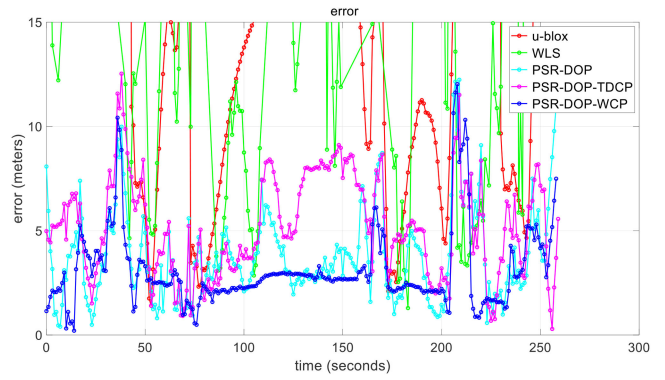


Fig. 8. Two-dimensional positioning errors of the evaluated five methods in urban canyon 2. The red curve denotes the 2-D error from the commercial solution of the u-blox receiver. The green, cyan, magenta, and blue colors denote the WLS, PSR-DOP, PSR-DOP-TDCP, and PSR-DOP-WCP, respectively.

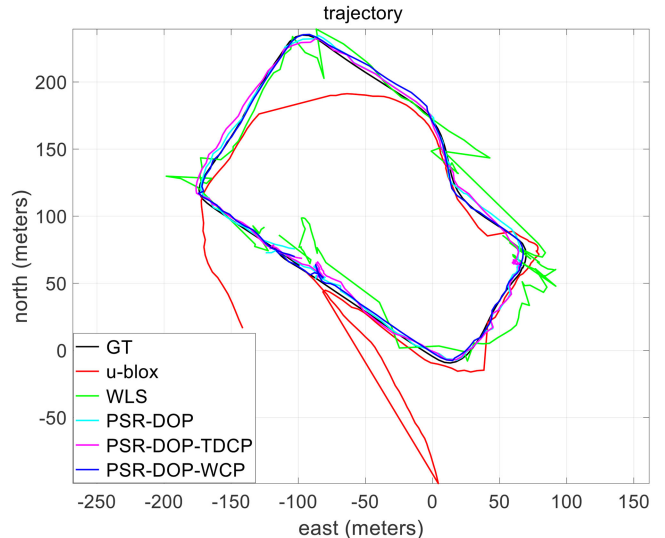


Fig. 9. Two-dimensional positioning trajectories of the evaluated five methods in urban canyon 2. The black and red curves denote the 2-D trajectories of the ground truth and the commercial solution of the u-blox receiver, respectively. The green, cyan, magenta, and blue colors denote the WLS, PSR-DOP, PSR-DOP-TDCP, and PSR-DOP-WCP, respectively.

improving the GNSS positioning even in such a dense urban canyon.

Fig. 9 shows the trajectories of the evaluated five methods. Both the solutions from the u-blox (red curve) and the WLS (green curve) deviate significantly from the ground truth (black curve) due to the GNSS outlier measurements. With the help of the proposed WCP constraint, a significantly smoother trajectory (blue curve) is obtained.

2) *Analysis of the Cycle Slip Accommodation via the M-Estimator:* As mentioned in Section IV-C, the cycle slip is accommodated by the M-estimator by mitigating the effects of the inconsistency in integer ambiguity. This is based on the assumption that the cycle slip can induce inconsistency in integer ambiguity where large residuals [see (17)] can be observed after solving (21). However, the performance of the M-estimator relies heavily on the selection of its

TABLE IV
Positioning Error of the PSR–DOP–WCP Under Different M-Estimator Setups in Urban Canyon 2

Item (m)	H (1)	H (2)	C (1)	C (2)	C (4)
MEAN	Diverge	Diverge	3.62	3.11	3.05
STD	Diverge	Diverge	2.04	1.78	1.68
Max	Diverge	Diverge	13.11	11.20	10.76

Note. H (1): Huber function with kernel value (k_ρ) of 1; C (1): Cauchy function with kernel value (k_ρ) of 1.

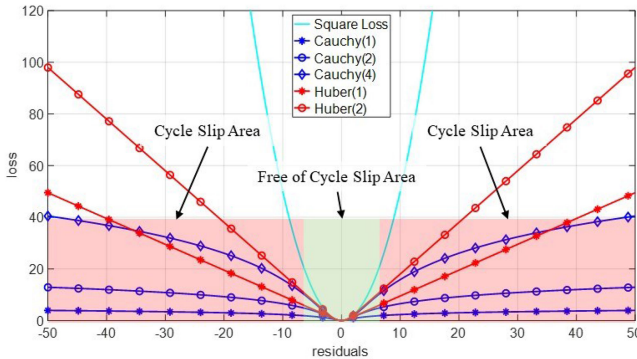


Fig. 10. Comparisons of the robust functions with different kernel values (k_ρ).

kernel parameter. To see how the selection of the kernel parameter impacts the performance of the proposed WCP with different kinds of M-estimators, Table IV presents the positioning performance of the proposed PSR–DOP–WCP under different M-estimator setups. The Huber-based M-estimator (see Appendix B regarding the formulation of the Huber function) fails to resist the inconsistency of integer ambiguity caused by the cycle slip for both selected kernel parameters where the PSR–DOP–WCP diverges. This is mainly due to the convex surface property of the Huber-based M-estimator. As a result, the Huber cannot mitigate the impacts of the gross outlier. The Huber and Cauchy functions with different kernel values (k_ρ) are shown in Fig. 10. The red-shaded area denotes the potential outlier area with larger residuals. The light green area denotes the typical healthy measurements area with smaller residuals. The cyan curve denotes the conventional squared loss function, where the gross outlier of the WCP constraint can cause large loss, leading to a large final position estimation error. The Huber-based robust function can mitigate the impacts of the outliers (e.g., the red curve) when compared with the conventional squared loss function. However, the outlier with a large residual can still mislead the final position estimation. For example, a residual of 50 can cause a loss of about 100 using the Huber (2), which can be seen by the red circle in Fig. 10. Differently, the Cauchy function is a cutoff function that can significantly mitigate the effects of the gross outlier. For example, a residual of 50 can cause a loss of only 4 using the Cauchy (1), which can be seen by the blue asterisk in Fig. 10. As a result, a mean error of 3.62 m is obtained using the Cauchy-based M-estimator with a kernel value of 1. The mean error decreases to 3.11 m with

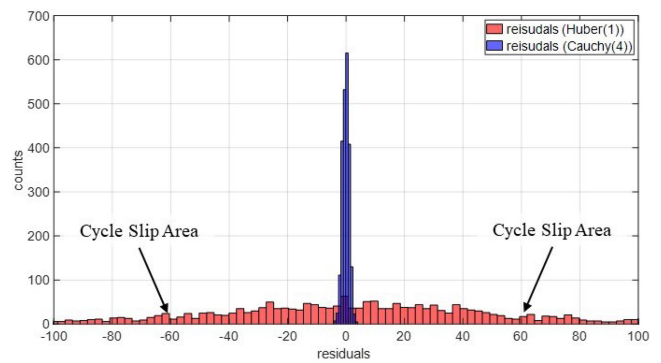


Fig. 11. Histograms of residuals of the WCP constraints using the Cauchy and Huber functions. The x-axis denotes the residuals calculated using (17), and the y-axis represents the counts.

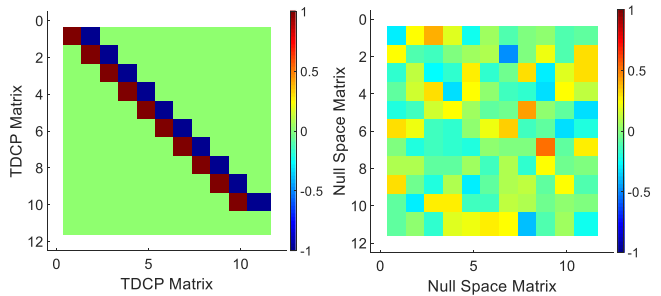


Fig. 12. Comparison of $\mathbf{D}_{r,k}^s$ for TDCP constraint and $\mathbf{G}_{r,k}^s$ for the proposed WCP constraint. The x- and y-axes denote the epoch index. The color denotes the value of the components of the matrix. The size of both matrices is 11×11 , where 11 denotes the number of epochs inside the window. In other words, the given satellite is continuously tracked for 11 epochs.

a kernel value of 2. A similar mean error is obtained after increasing the kernel value to 4, which is an appropriate kernel to accommodate the cycle slip phenomenon.

To show the detail of how the M-estimator helps to mitigate the impacts of the cycle slip phenomenon, in Fig. 11, we present the residuals of the WCP constraints in urban canyon 2, using Huber and Cauchy functions, respectively. With the help of the Cauchy function, the gross residuals are mitigated with all the residuals ranging between $[-4, 4]$. Conversely, the residuals involve a long tail with large values using the Huber function.

3) Analysis of the TDCP and Left Null Space Matrices:

As shown in the experimental results of urban canyons 1 and 2, the improved positioning results are obtained using the proposed WCP constraint based on $\mathbf{G}_{r,k}^s$, compared with the conventional TDCP constraint based on $\mathbf{D}_{r,k}^s$ [see (20)]. It is interesting to compare the difference between the two matrices with real data. To show the detail of the left null space matrix $\mathbf{G}_{r,k}^s$ of the WCP constraint and the TDCP matrix $\mathbf{D}_{r,k}^s$, we select a window for a satellite being observed for 11 epochs in the urban canyon 2. $\mathbf{G}_{r,k}^s$ of the WCP constraint is shown on the right side of Fig. 12. Similarly, $\mathbf{D}_{r,k}^s$ for the TDCP measurements is shown on the left side of Fig. 12. We can see that the off-diagonal components of $\mathbf{D}_{r,k}^s$ for the TDCP are zero, which neglects the cross-correlation between the multiple epochs of carrier-phase

TABLE V

Performance of the Listed Four Methods in an Urban Canyon Using a Smartphone-Level GNSS Receiver

Item (m)	WLS	Sol 1	Sol 2	Sol 3
MEAN	14.45	8.74	9.19	7.47
STD	11.79	4.21	4.82	4.60
Max	110.74	46.10	45.39	46.38

measurements. According to our previous work [19], the GNSS measurements are highly environmental dependent and time-correlated in urban scenarios. Differently, $\mathbf{G}_{r,k}^s$ for the proposed WCP is a dense matrix that effectively explores the correlation between measurements between consecutive epochs, which is the major difference between the proposed WCP and the conventional TDCP. As a result, the WCP constraint significantly increases the robustness of the estimator against outlier measurements and leads to smoother position estimation with the help of multiple epoch constraints.

D. Discussions: Experimental Evaluation in Urban Canyon Using a Low-Cost Smartphone-Level Receiver

The u-blox GNSS receiver and patch antenna belong to the automobile level that is usually used in intelligent transportation (ITS) application. Therefore, it is interesting to see how the proposed method works for the smartphone receiver. The internal antenna of a mobile phone is sensitive to multipath/NLOS, and the collected GNSS measurements are noisier. To this end, we collect the other dataset in an urban canyon. The applied smartphone is Huawei P40 Pro, and raw GPS/BeiDou measurements are collected at a frequency of 1 Hz. The positioning results of the listed four methods are shown in Table V. Since the NMEA solution from the smartphone is estimated based on additional information, such as onboard IMU, map matching [44], and magnetic sensors, we do not compare the NMEA solution in this experiment. A mean error of 14.45 m is obtained using the conventional WLS method, and the trajectory is shown in Fig. 13 with green curves. After applying the PSR-DOP method, the mean error decreases to 8.74 m, with a decreased standard deviation of 4.21 m. Interestingly, the mean error increases slightly to 9.19 m after applying the TDCP constraint. With the help of the proposed method, the mean error decreases to 7.47 m, which shows the effectiveness of the proposed method even in the low-cost smartphone-level GNSS receiver. However, we can see that the standard deviation even increases slightly after applying the WCP constraints compared with the PSR-DOP method. One of the major reasons is the unexpected cycle slip in carrier-phase measurements. Due to the limited cost of the GNSS receiver, the cases of the cycle slip are significantly increased compared with the ITS-level u-blox GNSS receiver. Although the Cauchy-based M-estimator can help to mitigate the impacts of the cycle slip, its impacts are still involved in the position estimation problem. It is important to detect the potential cycle slip with the help of other

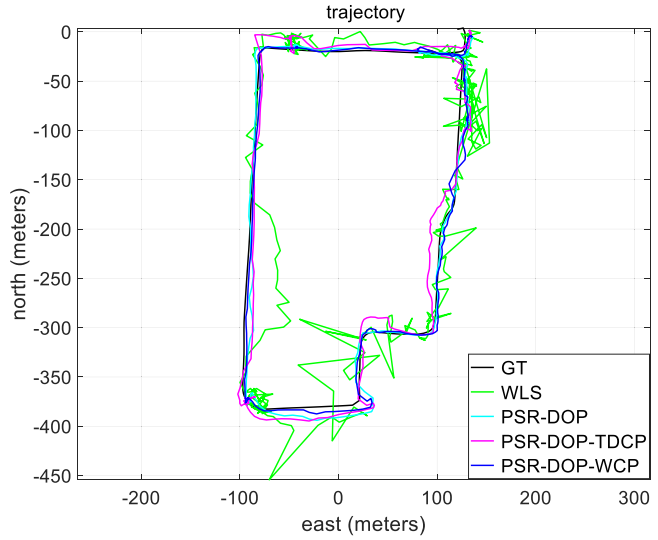


Fig. 13. Two-dimensional positioning trajectories of the evaluated four methods in an urban canyon. The black curve denotes the 2-D trajectories of the ground truth. The green, cyan, magenta, and blue colors denote the WLS, PSR-DOP (Sol 1), PSR-DOP-TDCP (Sol 2), and PSR-DOP-WCP (Sol 3), respectively.

additional onboard sensors, such as IMU, to further improve the proposed WCP constraint, which will be one of our future works.

E. Discussions: Performance Comparison of the Loosely and Tightly Integrated Doppler Measurements in FGO

Considering that the Doppler measurements are less sensitive to the multipath effects, this article integrates the Doppler measurements in a loosely coupled manner. Specifically, the velocity of the GNSS receiver is calculated first based on the WLS method [36]. Then, the estimated velocity is integrated with the pseudorange factor via (7). Compared with the tightly coupled integration of the Doppler measurements, the computational complexity of the loose integration of Doppler measurements is significantly decreased as only a single velocity factor is derived from the multiple Doppler frequency measurements. However, it is also interesting to see the difference in the positioning performance of the loosely and tightly coupled integration of the Doppler measurements.

A positioning comparison of the loosely and tightly coupled fusion of the pseudorange and Doppler measurements is shown in Fig. 14 based on the dataset collected in urban canyon 1. The details of the implementation of the tightly coupled integration of the Doppler and pseudorange measurements using FGO are presented in Appendix C. The positioning errors and used time per epoch are shown in Table VI. It can be seen that the positioning performance is slightly improved by using tightly coupled integration, where both the mean error and the standard deviation are slightly decreased. Meanwhile, the maximum error also decreases from 6.52 to 5.6 m. One of the major reasons is that the tightly coupled integration enables the modeling of the Doppler measurements in a more detailed way. The

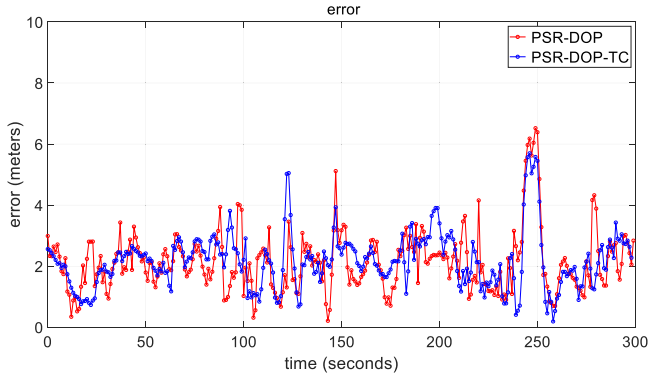


Fig. 14. Positioning performance comparison of the loosely and tightly coupled fusion of the pseudorange and Doppler measurements using the dataset collected in urban canyon 1.

TABLE VI

Performance Comparison of the Loosely and Tightly Coupled Fusion of the Pseudorange and Doppler Measurements Using the Dataset Collected in Urban Canyon 1

Item	PSR-DOP	PSR-DOP-TC
MEAN (meter)	2.14	2.01
STD (meter)	1.01	0.91
Max (meter)	6.52	5.6
Used Time Per Epoch (ms)	51	125

last row of Table VI shows the average used time for each epoch. It is shown that the used time is almost doubled by tightly coupled integration when compared with the loosely coupled integration.

F. Discussions: Performance Comparison of the Cycle Slip Mitigation Using the M-Estimator and Loop Lock Indicator

The loop lock indicator (LLI), which is directly outputted from the GNSS receiver, is one of the popular methods for cycle slip detection. In this section, we present the performance comparison of the different methods for cycle slip accommodation using the dataset collected in urban canyon 1. Specifically, we decode the GNSS raw data in receiver independent exchange [45] format and extract the LLI directly. Once the cycle slip is detected based on the LLI, a new WCP constraint will be generated. The following three methods are compared.

- 1) *M-estimator*: The implementation is based on PSR-DOP-TDCP, as illustrated in Section V-A, where the M-estimator is applied to mitigate the impacts of the cycle slips.
- 2) *LLI*: The implementation is based on PSR-DOP-TDCP, as illustrated in Section V-A. However, the M-estimator is not applied, and the LLI is applied to mitigate the impacts of the cycle slips.
- 3) *M-estimator-LLI*: The implementation is based on PSR-DOP-TDCP, as illustrated in Section V-A. Meanwhile, both the M-estimator and the LLI are applied to mitigate the impacts of the cycle slips.

TABLE VII
Performance Comparison of Different Methods for Cycle Slip Accommodation Based on the Dataset Collected in the Urban Canyon 1

Item (m)	M-estimator	LLI	M-estimator-LLI
MEAN	1.76	1.64	1.47
STD	0.57	0.53	0.56
Max	4.06	3.19	2.87

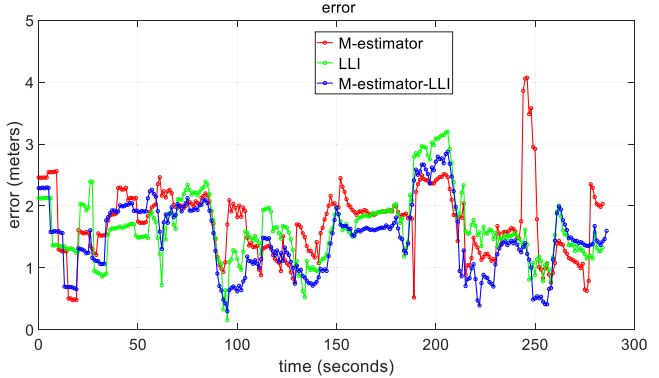


Fig. 15. Positioning errors comparison of different methods for cycle slip accommodation based on the dataset collected in the urban canyon 1.

The positioning results of the three listed methods for cycle slip accommodation are shown in Table VII. Interestingly, better positioning accuracy is obtained compared with the M-estimator-based cycle slip accommodation method, with the mean error decreasing from 1.76 to 1.64 m, if the LLI-based cycle slip detection is applied. The results implicate that the LLI is an effective indicator for cycle slip detection. Interestingly, a further improved positioning result is obtained by combining both the LLI and the M-estimator for the accommodation of the cycle slip with a mean error of 1.47 m. Moreover, both the STD and the Max. error are decreased slightly. The detailed errors associated with the listed three methods are shown in Fig. 15. The results show that the M-estimator can further help to mitigate the impacts of the missed cycle slip detection by the LLI.

VI. CONCLUSION

Accurate GNSS positioning in urban canyons is still a challenging problem due to excessive outlier measurements caused by the surrounding high-rising building structures. To improve urban GNSS positioning, instead of relying on the TDCP, which only considers two neighboring epochs using an EKF estimator, this article proposed to employ the carrier-phase measurements inside a window, the so-called WCP, to constrain the states inside a factor graph. The effectiveness of the proposed method is verified using both automobile-level and smartphone-level GNSS receivers in the typical urban canyons of Hong Kong.

One of the major limitations of the proposed method is the reliance on the assumption of constant integer ambiguity for the continuously observed carrier-phase measurements. Although the M-estimator and the LLI are employed for the accommodation of the cycle slip phenomenon, missed cycle slip detection can still occur. In the future, we will

study the detection of cycle slips by adding the occurrence of the cycle slip as an additional state to be estimated with the help of data redundancy inside the FGO. Moreover, we will also integrate the proposed GNSS positioning method with additional sensors.

APPENDIX

A. CONSTRUCTION OF THE LEFT NULL SPACE MATRIX

Given a vector $\mathbf{v}_{r,k}^s = [1 \ 1 \ \dots \ 1]^T$, there are several candidate matrices $\mathbf{G}_{r,k}^s$ that satisfy the following equation:

$$\mathbf{G}_{r,k}^s \begin{bmatrix} 1 \\ 1 \\ \dots \\ 1 \end{bmatrix} = \begin{bmatrix} 0 \\ 0 \\ \dots \\ 0 \end{bmatrix}. \quad (23)$$

Theoretically, $\mathbf{G}_{r,k}^s$ encodes the time correlation of the carrier-phase measurements considered in a WCP by using (15). Different selections of $\mathbf{G}_{r,k}^s$ correspond to different confidence levels of time correlation across different epochs of carrier-phase measurements. However, it is still an open question that how to select the optimal $\mathbf{G}_{r,k}^s$ that can optimally capture the time correlation inside the WCP.

According to our evaluation in Section V, the performance of the WCP is mainly dominated by the size of the window (N_k^s) and the quality of the covariance estimation ($\Sigma_{r,k}^{WCP,s}$). Therefore, we adopt the random process [46] to construct $\mathbf{G}_{r,k}^s$ based on the given size of the window denoted by N_k^s . First, the orthonormal basis [46] of the null space of the matrix \mathbf{v} can be calculated, which is denoted by matrix $\mathbf{S}_{r,k}^s$. Then, a complex matrix $\mathbf{H}_{r,k}^s$ can be constructed by randomly generating two matrices $\mathbf{H}_{r,k,1}^s$ and $\mathbf{H}_{r,k,2}^s$, which make up the real and imaginary parts of matrix $\mathbf{H}_{r,k}^s = [\mathbf{H}_{r,k,1}^s \ \mathbf{H}_{r,k,2}^s]$. Meanwhile, all the components of the two matrices $\mathbf{H}_{r,k,1}^s$ and $\mathbf{H}_{r,k,2}^s$ range between [0, 1]. Then, the QR factorization [46] is performed as follows:

$$\mathbf{Q}_{r,k}^s \ \mathbf{R}_{r,k}^s = [\mathbf{H}_{r,k}^s - \mathbf{I}_{r,k}^s] \quad (24)$$

where the matrix $\mathbf{Q}_{r,k}^s$ is an orthogonal matrix and the matrix $\mathbf{R}_{r,k}^s$ is an upper triangular matrix. Finally, a unitary matrix can be generated as follows:

$$\mathbf{U}_{r,k}^s = \mathbf{S}_{r,k}^s \ \mathbf{Q}_{r,k}^s \mathbf{S}_{r,k}^{s\top} + \frac{1}{N_k^s} \mathbf{v}_{r,k}^s \mathbf{v}_{r,k}^{s\top} \quad (25)$$

where $\mathbf{U}_{r,k}^s$ is a complex and unitary matrix. Finally, $\mathbf{G}_{r,k}^s$ is the imaginary part of the matrix $\mathbf{U}_{r,k}^s$.

B. Huber-Based Robust Function for the WCP Constraint

Given the error function of the WCP constraint as $\mathbf{e}_{r,k}^{WCP,s}$, the robustified Huber-based error function can be formulated as follows:

$$\rho(\mathbf{e}_{r,k}^{WCP,s}) = \begin{cases} \frac{1}{2}(c)^2, & |\mathbf{e}_{r,k}^{WCP,s}| \leq k_\rho \\ k_\rho \left(|\mathbf{e}_{r,k}^{WCP,s}| - \frac{1}{2}k_\rho \right), & |\mathbf{e}_{r,k}^{WCP,s}| > k_\rho \end{cases} \quad (26)$$

where k_ρ denotes the kernel value (parameter).

C. Tightly Coupled Integration of Pseudorange/Doppler Integration

Different from the loosely coupled integration, the receiver clock bias drift should also be estimated simultaneously in the tightly coupled integration. The state of the GNSS receiver at a single epoch can be denoted as follows:

$$\mathbf{x}_{r,t} = (\mathbf{p}_{r,t}, \mathbf{v}_{r,t}, \delta_{r,t}, \dot{\delta}_{r,t})^T \quad (27)$$

where $\mathbf{x}_{r,t}$ denotes the state of the GNSS receiver at epoch t , $t \in (1, n)$, which involves the position ($\mathbf{p}_{r,t}$), velocity ($\mathbf{v}_{r,t}$), receiver clock bias ($\delta_{r,t}$), and receiver clock bias drift ($\dot{\delta}_{r,t}$). The range rate measurement vector ($\mathbf{y}_{r,t}^d$) at an epoch t is expressed as follows:

$$\mathbf{y}_{r,t}^d = (\lambda d_{r,t}^1, \lambda d_{r,t}^2, \lambda d_{r,t}^3, \dots)^T \quad (28)$$

where λ denotes the carrier wavelength, and $d_{r,t}^s$ represents the Doppler measurements. The observation function $\mathbf{h}^d(*)$, which connects the state and the Doppler measurements, is expressed as follows:

$$\mathbf{h}^d(\mathbf{x}_t^d) = \begin{bmatrix} rr_{r,t}^1 + \dot{\delta}_{r,t} - \dot{\delta}_{r,t}^1 \\ rr_{r,t}^2 + \dot{\delta}_{r,t} - \dot{\delta}_{r,t}^2 \\ rr_{r,t}^3 + \dot{\delta}_{r,t} - \dot{\delta}_{r,t}^3 \\ \vdots \\ rr_{r,t}^m + \dot{\delta}_{r,t} - \dot{\delta}_{r,t}^m \end{bmatrix} \quad (29)$$

where the superscript S denotes the total number of satellites. The variable $rr_{r,t}^s$ denotes the expected range rate. The variables $\dot{\delta}_{r,t}$ and $\dot{\delta}_{r,t}^s$ represent the receiver and satellite clock bias drift, respectively. The line-of-sight vector of the given satellite s can be denoted as follows:

$$\mathbf{k}_{r,t}^s = \left(\frac{\mathbf{p}_{t,x}^s - \mathbf{p}_{r,t,x}}{\|\mathbf{p}_t^s - \mathbf{p}_{r,t}\|}, \frac{\mathbf{p}_{t,y}^s - \mathbf{p}_{r,t,y}}{\|\mathbf{p}_t^s - \mathbf{p}_{r,t}\|}, \frac{\mathbf{p}_{t,z}^s - \mathbf{p}_{r,t,z}}{\|\mathbf{p}_t^s - \mathbf{p}_{r,t}\|} \right)^T \quad (30)$$

The expected range rate $rr_{r,t}^s$ for satellite s can also be calculated as follows:

$$rr_{r,t}^s = \mathbf{k}_{r,t}^s (\mathbf{v}_t^s - \mathbf{v}_{r,t}) + \frac{\omega_{earth}}{c_L} (\mathbf{v}_{t,y}^s \mathbf{p}_{r,t,x} + \mathbf{p}_{t,y}^s \mathbf{v}_{r,t,x} + \mathbf{p}_{t,x}^s \mathbf{v}_{r,t,y}) \quad (31)$$

where variable ω_{earth} [34] denotes the angular velocity of the earth's rotation. Variable c_L denotes the speed of the light.

The range rate measurements $\mathbf{y}_{r,t}^d$ at a given epoch t can be derived from (28), and the expected range rate $rr_{r,t}^s$ for satellite s can be derived from (31). Therefore, we can get the error function ($\mathbf{e}_{r,t}^D$) for a given satellite measurement $\lambda d_{r,t}^s$ as follows:

$$\|\mathbf{e}_{r,t}^D\|_{\Sigma_{r,t}^D}^2 = \|\lambda d_{r,t}^s - rr_{r,t}^s\|_{\Sigma_{r,t}^D}^2 \quad (32)$$

where $\Sigma_{r,t}^D$ denotes the covariance matrix that is calculated based on the elevation angle and SNR [35]. Therefore, the objective function for the tightly coupled GNSS positioning

using FGO is formulated as follows:

$$\chi^* = \arg \min_{\chi} \sum_{s,k} \left(\|\mathbf{e}_{r,t}^D\|_{\Sigma_{r,t}^D}^2 + \|\mathbf{e}_{r,t}^s\|_{\Sigma_{r,t}^s}^2 + \|\mathbf{e}_{r,t}^{DV}\|_{\Sigma_{r,t}^{DV}}^2 \right) \quad (33)$$

The variable χ^* denotes the optimal estimation of the state sets, which includes $\mathbf{x}_{r,t}$ from multiple epochs. The variable s denotes the index of the satellite of epoch t . The state set χ^* can be estimated by solving the objective function (33). In short, the factor ($\mathbf{e}_{r,t}^D$) from the raw Doppler measurement is employed to constrain the estimation of the velocity of the GNSS receiver. The factor ($\mathbf{e}_{r,t}^s$) from the pseudorange measurement is employed to constrain the position of the GNSS receiver. The factor ($\mathbf{e}_{r,t}^{DV}$) works as a constant-velocity-based motion model to connect the states from two consecutive epochs. Note that the carrier phase is not applied in this tightly coupled integration.

REFERENCES

- [1] P. K. Enge
The global positioning system: Signals, measurements, and performance
Int. J. Wireless Inf. Netw., vol. 1, no. 2, pp. 83–105, 1994.
- [2] W. Wen *et al.*
Urbanloco: A full sensor suite dataset for mapping and localization in urban scenes
In *Proc. IEEE Int. Conf. Robot. Automat.*, 2020, pp. 2310–2316.
- [3] Y. Ng and G. X. Gao
GNSS multireceiver vector tracking
IEEE Trans. Aerosp. Electron. Syst., vol. 53, no. 5, pp. 2583–2593, Oct. 2017.
- [4] M. Wildemeersch, C. H. Slump, and A. Rabbachin
Acquisition of GNSS signals in urban interference environment
IEEE Trans. Aerosp. Electron. Syst., vol. 50, no. 2, pp. 1078–1091, Apr. 2014.
- [5] S.-H. Kong
Statistical analysis of urban GPS multipaths and pseudo-range measurement errors
IEEE Trans. Aerosp. Electron. Syst., vol. 47, no. 2, pp. 1101–1113, Apr. 2011.
- [6] W. Wen, G. Zhang, and L.-T. Hsu
Exclusion of GNSS NLOS receptions caused by dynamic objects in heavy traffic urban scenarios using real-time 3D point cloud: An approach without 3D maps
In *Proc. Position, Location Navigat. Symp.*, 2018, pp. 158–165.
- [7] Z. Zhang, H. Yuan, B. Li, X. He, and S. Gao
Feasibility of easy-to-implement methods to analyze systematic errors of multipath, differential code bias, and inter-system bias for low-cost receivers
GPS Solutions, vol. 25, no. 3, pp. 1–14, 2021.
- [8] A. Pirsavash, A. Broumandan, and G. Lachapelle
Characterization of signal quality monitoring techniques for multipath detection in GNSS applications
Sensors, vol. 17, no. 7, 2017, Art. no. 1579.
- [9] L. Wang, P. D. Groves, and M. K. Ziebart
Urban positioning on a smartphone: Real-time shadow matching using GNSS and 3D city models
In *Proc. 26th Int. Tech. Meeting Satell. Division Inst. Navigat.*, 2013, pp. 1606–1619.
- [10] L. Wang, P. D. Groves, and M. K. Ziebart
Smartphone shadow matching for better cross-street GNSS positioning in urban environments
J. Navigat., vol. 68, no. 3, pp. 411–433, 2015.
- [11] H.-F. Ng, G. Zhang, and L.-T. Hsu
A computation effective range-based 3D mapping aided GNSS with NLOS correction method
J. Navigat., vol. 73, no. 6, pp. 1202–1222, 2020.
- [12] X. Bai, W. Wen, and L.-T. Hsu
Using sky-pointing fish-eye camera and LiDAR to aid GNSS single-point positioning in urban canyons
IET Intell. Transport Syst., vol. 14, no. 8, pp. 908–914, 2020.
- [13] J. i. Meguro, T. Murata, J. i. Takiguchi, Y. Amano, and T. Hashizume
GPS multipath mitigation for urban area using omnidirectional infrared camera
IEEE Trans. Intell. Transp. Syst., vol. 10, no. 1, pp. 22–30, Mar. 2009.
- [14] W. Wen, X. Bai, Y. C. Kan, and L.-T. Hsu
Tightly coupled GNSS/INS integration via factor graph and aided by fish-eye camera
IEEE Trans. Veh. Technol., vol. 68, no. 11, pp. 10651–10662, Nov. 2019.
- [15] W. Wen, G. Zhang, and L. T. Hsu
Correcting NLOS by 3-D LiDAR and building height to improve GNSS single point positioning
Navigat., vol. 66, no. 4, pp. 705–718, 2019.
- [16] Z. Tao and P. Bonnifait
Sequential data fusion of GNSS pseudoranges and Dopplers with map-based vision systems
IEEE Trans. Intell. Veh., vol. 1, no. 3, pp. 254–265, Sep. 2016.
- [17] W. Wen, T. Pfeifer, X. Bai, and L.-T. Hsu
Factor graph optimization for GNSS/INS integration: A comparison with the extended Kalman filter
Navigat. J. Inst. Navigat., vol. 68, no. 2, pp. 315–331, 2021.
- [18] Z. Zhang, B. Li, and Y. Shen
Efficient approximation for a fully populated variance-covariance matrix in RTK positioning
J. Surveying Eng., vol. 144, no. 4, 2018, Art. no. 04018005.
- [19] W. Wen and L.-T. Hsu
Towards robust GNSS positioning and real-time kinematic using factor graph optimization
In *Proc. IEEE Int. Conf. Robot. Automat. (ICRA)*, 2021, pp. 5884–5890.
- [20] Z. Zhang, B. Li, Y. Gao, and Y. Shen
Real-time carrier phase multipath detection based on dual-frequency C/N0 data
GPS Solutions, vol. 23, no. 1, pp. 1–13, 2019.
- [21] P. Teunissen
Theory of integer equivariant estimation with application to GNSS
J. Geodesy, vol. 77, no. 7/8, pp. 402–410, 2003.
- [22] P. Teunissen and A. Khodabandeh
Review and principles of PPP-RTK methods
J. Geodesy, vol. 89, no. 3, pp. 217–240, 2015.
- [23] P. Freda, A. Angrisano, S. Gaglione, and S. Troisi
Time-differenced carrier phases technique for precise GNSS velocity estimation
GPS Solutions, vol. 19, no. 2, pp. 335–341, 2015.
- [24] J. Kim *et al.*
A low-cost, high-precision vehicle navigation system for deep urban multipath environment using TDCP measurements
Sensors, vol. 20, no. 11, 2020, Art. no. 3254.
- [25] K.-W. Chiang, Y.-H. Li, L.-T. Hsu, and F.-Y. Chu
The design a TDCP-Smoothed GNSS/Odometer integration scheme with vehicular-motion constraint and robust regression
Remote Sens., vol. 12, no. 16, 2020, Art. no. 2550.
- [26] N. Qian *et al.*
Vehicle's instantaneous velocity reconstruction by combining GNSS Doppler and carrier phase measurements through Tikhonov regularized kernel learning

- [27] G. Chang, N. Qian, C. Chen, and J. Gao
Precise instantaneous velocimetry and accelerometry with a stand-alone GNSS receiver based on sparse kernel learning
Measurement, vol. 159, 2020, Art. no. 107803.
- [28] L. Zhang, G. Chang, C. Chen, S. Zhang, and T. Zhu
GNSS velocimeter by adaptively combining carrier phase and Doppler measurements
IET Sci., Meas. Technol., vol. 14, no. 7, pp. 762–771, 2020.
- [29] T. Suzuki
Time-relative RTK-GNSS: GNSS loop closure in pose graph optimization
IEEE Robot. Automat. Lett., vol. 5, no. 3, pp. 4735–4742, Jul. 2020.
- [30] M. Li and A. I. Mourikis
High-precision, consistent EKF-based visual-inertial odometry
Int. J. Robot. Res., vol. 32, no. 6, pp. 690–711, 2013.
- [31] S. Zhao, Y. Chen, and J. A. Farrell
High-precision vehicle navigation in urban environments using an MEM's IMU and single-frequency GPS receiver
IEEE Trans. Intell. Transp. Syst., vol. 17, no. 10, pp. 2854–2867, Oct. 2016.
- [32] D. E. Tyler
A distribution-free M-estimator of multivariate scatter
Ann. Statist., vol. 15, pp. 234–251, 1987.
- [33] E. Kaplan and C. Hegarty
Understanding GPS: Principles and Applications. Norwood, MA, USA: Artech house, 2005.
- [34] T. Takasu and A. Yasuda
Development of the low-cost RTK-GPS receiver with an open source program package RTKLIB
In *Proc. Int. Symp. GPS/GNSS*, 2009, pp. 4–6.
- [35] A. M. Herrera, H. F. Suhandri, E. Realini, M. Reguzzoni, and M. C. de Lacy
goGPS: Open-source MATLAB software
GPS Solutions, vol. 20, no. 3, pp. 595–603, 2016.
- [36] B. Hofmann-Wellenhof, H. Lichtenegger, and E. Wasle
GNSS—Global Navigation Satellite Systems: GPS, GLONASS, Galileo, and More. Berlin, Germany: Springer, 2007.
- [37] X. Bai, W. Wen, and L.-T. Hsu
Robust visual-inertial integrated navigation system aided by online sensor model adaption for autonomous ground vehicles in urban areas
Remote Sens., vol. 12, no. 10, 2020, Art. no. 1686.
- [38] S. Agarwal and K. Mierle
Ceres solver: Tutorial & reference
Google Inc., vol. 2, no. 72, p. 8, 2012.
- [39] L.-T. Hsu *et al.*
UrbanNav: An open-sourced multisensory dataset for benchmarking positioning algorithms designed for urban areas (Accepted)
In *Proc. Int. Tech. Meeting Satell. Division Inst. Navigat.*, 2021, pp. 226–256.
- [40] M. Quigley *et al.*
ROS: An open-source robot operating system
in presented at the *ICRA Workshop Open Source Softw.*, Kobe, Japan, 2009, vol. 3, pp. 1–6.
- [41] M. Taufik, M. Cahyadi, and J. Putra
Analysis level of accuracy GNSS observation processing using u-blox as low-cost GPS and geodetic GPS (case study: M8T)
IOP Conf. Ser.: Earth Environ. Sci., vol. 389, no. 1, 2019, Art.no. 012041.
- [42] P. D. Groves
Principles of GNSS, Inertial, and Multisensor Integrated Navigation Systems. Norwood, MA, USA: Artech house, 2013.
- [43] P. Xie and M. G. Petovello
Measuring GNSS multipath distributions in urban canyon environments
IEEE Trans. Instrum. Meas., vol. 64, no. 2, pp. 366–377, Feb. 2015.
- [44] E. Algizawy, T. Ogawa, and A. El-Mahdy
Real-time large-scale map matching using mobile phone data
ACM Trans. Knowl. Discov. Data, vol. 11, no. 4, pp. 1–38, 2017.
- [45] W. Gurtner and L. Estey
RINEX—The Receiver Independent Exchange Format—Version 3.00. Boulder, CO, USA: UNAVCO, 2007.
- [46] D. S. Watkins
Fundamentals of Matrix Computations. Hoboken, NJ, USA: Wiley, 2004.



Xiwei Bai received the M.Sc. degree in engineering from China Agricultural University, Beijing, China, in 2018. She is currently working toward the Ph.D. degree in mechanical engineering with Hong Kong Polytechnic University, Hong Kong.

From 2018 to 2019, she was a Research Assistant with Hong Kong Polytechnic University. Her research interests include visual simultaneous localization and mapping and vision-aided global navigation satellite system positioning in urban canyons for the intelligent transportation system and autonomous driving.



Weisong Wen was born in Ganzhou, China. He received the Ph.D. degree in mechanical engineering from Hong Kong Polytechnic University, Hong Kong, in 2020.

He was a Visiting Student Researcher with the University of California, Berkeley in 2018. He is currently a Research Assistant Professor with the Department of Aeronautical and Aviation Engineering, Hong Kong Polytechnic University. His research interests include multisensor integrated localization for autonomous vehicles, visual simultaneous localization and mapping, and vision-aided global navigation satellite system positioning in urban canyons.



Li-Ta Hsu received the B.S. and Ph.D. degrees in aeronautics and astronautics from National Cheng Kung University, Tainan, Taiwan, in 2007 and 2013, respectively.

He is currently an Associate Professor with the Department of Aeronautical and Aviation Engineering, Hong Kong Polytechnic University, Hong Kong. He was a Postdoctoral Researcher with the Institute of Industrial Science, University of Tokyo, Tokyo, Japan. In 2012, he was a Visiting Scholar with University College

London, London, U.K. His research interests include global navigation satellite system positioning in challenging environments and localization for pedestrians, autonomous driving vehicles, and unmanned aerial vehicles.